

Optimal Spatial Anomaly Detection

Baiyu Wang and Chao Zheng

October 20, 2025

Abstract

There has been a growing interest in anomaly detection problems recently, whilst their focuses are mostly on anomalies taking place on the time index. In this work, we investigate a new anomaly-in-mean problem in multidimensional spatial lattice, that is, to detect the number and locations of anomaly “spatial regions” from the baseline. In addition to the classic minimisation over the cost function with a L_0 penalisation, we introduce an innovative penalty on the area of the minimum convex hull that covers the anomaly regions. We show that the proposed method yields a consistent estimation of the number of anomalies, and it achieves near optimal localisation error under the minimax framework. We also propose a dynamic programming algorithm to solve the double penalised cost minimisation approximately, and carry out large-scale Monte Carlo simulations to examine its numeric performance. The method has a wide range of applications in real-world problems. As an example, we apply it to detect the marine heatwaves using the sea surface temperature data from the European Space Agency.

Keywords: Anomaly detection; Dynamic programming; Minimax optimality; Penalised cost; Spatial lattice

1 Introduction

Anomaly detection is a long-standing challenge in engineering, physics, and social sciences, concerned with identifying observations whose values are statistically improbable compared to a given baseline distribution. In many practical applications, anomalies arise

in data that are indexed by spatial locations, for example, detecting colorectal cancer by searching tumour regions in histology slides (Gu et al., 2023); segmenting anomalous areas corresponding to deforestation and burn scars in multi-source satellite imagery (Fodor and Conde, 2023); finding burglary hotspots through crime rates in cities (Kalantari et al., 2020). In these problems, an anomaly often refers to a collection of points or units on a spatial map, forming regions with possibly very complex shapes.

As a motivating example of this work, oceanographers and climate scientists are interested in studying marine heatwaves (MHWs), which are prolonged, extreme, extensive, and persistent warm water events that occur in the upper layers of the ocean (Chapman et al., 2022; Holbrook et al., 2020). Accurately identifying anomalous oceanic regions affected by MHWs, by recovering their locations and spatial extents, is essential for effective monitoring, resource management, and climate impact assessment. This task is challenging especially because the MHW regions have arbitrary and differing spatial shapes, which could be highly non-convex, with internal holes, and consisting of multiple disconnected components. To address this challenge, we propose a new methodology that can implement automatic detection of complex spatial anomaly regions corresponding to MHW events.

There are several existing attempts to address the spatial anomaly detection (SAD) problem, including those based on scan statistics (Kulldorff, 1997; Li et al., 2011; Patil and Taillie, 2003; Tango and Takahashi, 2005; Zhang et al., 2010), which often fail to accommodate multiple anomalies with complex shapes, and lack theoretical guarantees such as detection consistency. Graph-cut methods (Boykov and Funka-Lea, 2006) do not impose topological constraints on the anomaly region, but are limited to detecting a single anomalous region relative to a baseline. More recently, deep learning techniques (Hansen et al., 2022; Ronneberger et al., 2015; Wan et al., 2022) have been introduced to solve related problems. However, these methods usually focus on identifying outliers at the individual point or unit level, which contrasts with the objective of SAD in our study. Moreover, deep learning models generally require a large number of training datasets, which are not available in most real-world applications.

We take inspirations from recent techniques in changepoint detection literature, most of which consider a time-indexed sequence of observations $\{Y_t\}_{t=1}^n$ (Killick et al., 2012; Wang et al., 2020) and seek a set of changepoints $\{\tau_1, \dots, \tau_m\} \subset \{1, \dots, n\}$ on the time indices that partition the sequence into $m + 1$ homogeneous segments. Within each segment, the data are typically assumed to follow a common structure, whereas adjacent segments exhibit distinct structural properties.

Direct application of existing changepoint detection methods to SAD is nontrivial, as the spatial scenario fundamentally differs from the timeline setting, particularly when the anomaly regions may exhibit arbitrarily complex geometric and topological structures in general dimensions. In the timeline setting, each segment can be fully characterised by two boundary points. In contrast, identifying spatial regions is substantially more intricate. For instance, when a region has highly irregular boundaries, it may occur that every point on the region is effectively a boundary point. Consequently, SAD necessitates identifying all points within the anomaly region, rather than relying on a small number of boundary points. Furthermore, note that unlike the time index, spatial locations lack a natural total ordering. A large class of sequential timeline detection methods that rely on the search for changepoints along a predefined direction or path, including binary segmentation (Venkatraman, 1992; Vostrikova, 1981) and its variants (Cho and Fryzlewicz, 2015; Fryzlewicz, 2014; Kovács et al., 2023), are not applicable. Similarly, efficient computational algorithms such as PELT (Killick et al., 2012), which achieve linear computational cost by sequentially removing candidate changepoints from future iterations when pruning conditions are met, are also not suitable for the SAD problem. Although artificial orderings, such as row- or column-major order, or partial order based on half- or quarter-plane constructions, can be imposed on spatial data, these do not fundamentally resolve the abovementioned problems.

A number of studies have extended timeline changepoint detection to a spatial-temporal scenario, while still assuming that changepoints take place in the temporal domain. For example, Gromenko et al. (2017) develops Cramér–von Mises-type of tests to detect single changepoints under a functional data analysis framework. Moore et al. (2025) employs a scan statistic to sequentially detect distributional changes occurring over time in spatially clustered regions. Zhao et al. (2024) proposes a composite likelihood–MDL approach to simultaneously estimate multiple changepoints, thereby partitioning the data into piecewise stationary spatio-temporal processes. In the spatial setting, Chan et al. (2022) studies the discrepancy-based statistic over small blocks to identify the boundary of regions with structural change, while Kirch et al. (2025) develops a method based on contrasts of local-window means to localise spatial anomaly regions in image data. However, these approaches focus solely on identifying the locations of a regional change and do not address the problem of determining the number of such changes. Madrid Padilla et al. (2021) applies dyadic classification and regression trees (DCART) to partition the spatial lattice into multiple piecewise constant mean regions under constraints on partition complexity. In a related work, Yu et al. (2022) generalises this framework from regular lattices to graph data.

In this paper, we develop an anomaly-in-mean model on spatial lattice and propose an

innovative double penalised least squares approach for spatial anomaly detection (DPLS-SAD). Our anomaly regions are defined as sets of spatial grid points sharing a common mean signal, which differs from that of the baseline region. We provide theoretical guarantees for the consistent detection of anomaly regions with complex geometry, e.g., irregular shapes, internal holes, and disconnected components, including recovering their number and locations within an error bound that attains the minimax optimal rate up to a logarithm factor. In addition, we address the computational challenges associated with solving the inherently non-convex and NP-hard optimisation problem. To this end, we develop a dynamic programming-based search strategy that substantially improves computational efficiency, reducing the complexity from exponential to polynomial in the sample size.

The remainder of the paper is organised as follows. Section 2 introduces the model setup and the new double penalised cost function. Section 3 establishes theoretical guarantees for DPLS-SAD, followed by minimax optimal localisation rate analysis in Section 4. Section 5 extends our spatial anomaly detection problem to more general settings, including multi-dimensional and spatially dependent data. Sections 6 and 7 present the proposed algorithm and simulation studies. Section 8 applies our method to detect marine heatwave events (MHW) from the sea surface temperature (SST) data provided by the European Space Agency. Additional simulation results and technical proofs are deferred to the Supplementary Material.

2 Detection of spatial anomalies

In this section, we first propose the model setup for detecting spatial anomalies under an anomaly-in-mean setting, and introduce the quantities of interest, such as the number and “locations” of spatial anomaly regions. We then present a new double penalised cost function for estimating spatial anomaly regions, which imposes penalties on both the number of anomalies and the cardinality of their minimum convex hulls.

2.1 Model setup and spatial anomalies

Consider a univariate process $\{Y(\mathbf{s}) : \mathbf{s} \in \mathcal{S}, \mathcal{S} \subset \mathbb{R}^2\}$ indexed by the set \mathcal{S} , which are locations on a regular 2D lattice. Note that all of our methodology and theoretical results can be generalised to higher-dimensional settings, i.e., $\mathcal{S} = \{(s_1, s_2, \dots, s_d)\} \subset \mathbb{R}^d$, which will be discussed in Section 5.

Suppose $Y(\mathbf{s})$ can be decomposed into two components:

$$Y(\mathbf{s}) = \mu(\mathbf{s}) + \varepsilon(\mathbf{s}), \quad \mathbf{s} \in \{1, 2, \dots, n_1\} \times \{1, 2, \dots, n_2\},$$

where n_1 and n_2 are the lengths of the realised process on the horizontal and vertical coordinates, respectively. The total sample size is $n = n_1 \times n_2$. Without loss of generality, we may assume n is a square number and $n_1 = n_2 = \sqrt{n}$. In Section 5, we also extend the results to the case where the dimensions of \mathcal{S} diverge at different rates, i.e., $n_1 \neq n_2$.

The signal component $\{\mu(\mathbf{s})\}_{\mathbf{s} \in \mathcal{S}}$ are deterministic, on which the anomalies take place. The stochastic error component $\{\varepsilon(\mathbf{s})\}_{\mathbf{s} \in \mathcal{S}}$ are assumed to be independent sub-Gaussian, as specified in Assumption 1 below, which is a standard assumption made in many existing timeline changepoint/anomaly detection literature.

Assumption 1. (Sub-Gaussian errors) *The errors $\{\varepsilon(\mathbf{s})\}_{\mathbf{s} \in \mathcal{S}}$ are independent centered sub-Gaussian random variables with $\|\varepsilon(\mathbf{s})\|_{\psi_2}^2 \leq \sigma^2$ for all $\mathbf{s} \in \mathcal{S}$.*

Here $\|\cdot\|_{\psi_2}$ denotes the Orlicz- ψ_2 norm, i.e., $\|\varepsilon(\mathbf{s})\|_{\psi_2} = \inf\{t > 0, \mathbb{E}e^{\varepsilon(\mathbf{s})^2/t^2} \leq 2\}$. Note that the independent error assumption may not be suitable for many spatial applications. We relax this assumption and extend our analysis to spatially correlated data in Section 5.

Assume that the spatial lattice \mathcal{S} can be partitioned into $m+1$ non-overlapping regions: a baseline region R_0 and m anomaly regions, i.e., R_1, R_2, \dots, R_m , such that $\mu(\mathbf{s})$ is invariant within each anomaly region, while being different from the baseline region:

$$\mu(\mathbf{s}) = \mu_j, \quad \forall \mathbf{s} \in R_j \quad \text{and} \quad \mu_j \neq \mu_0, \quad j = 1, \dots, m.$$

In this way, $\mu(\mathbf{s})$ is a region-wise constant mean signal. Note that the mean signals within different anomaly regions can be close or even identical to each other. The number of anomaly regions m , their partitions $\{R_1, \dots, R_m\}$, and the mean signals $\{\mu_1, \dots, \mu_m\}$ are unknown, which are the quantities of interest in this problem.

The anomalies $\{R_1, \dots, R_m\}$ here are defined as spatial regions, which are essentially collections of grid points, see Figure 1 below. This is similar in spirit to the concept of collective anomalies (Fisch et al., 2022) in the timeline setting (when $d = 1$), where each timeline anomaly is an interval and can be identified by its endpoints. However, as discussed in Section 1, “boundary” points are not particularly useful for spatial anomalies, and in the SAD problem, we must instead specify all grid points within the region.

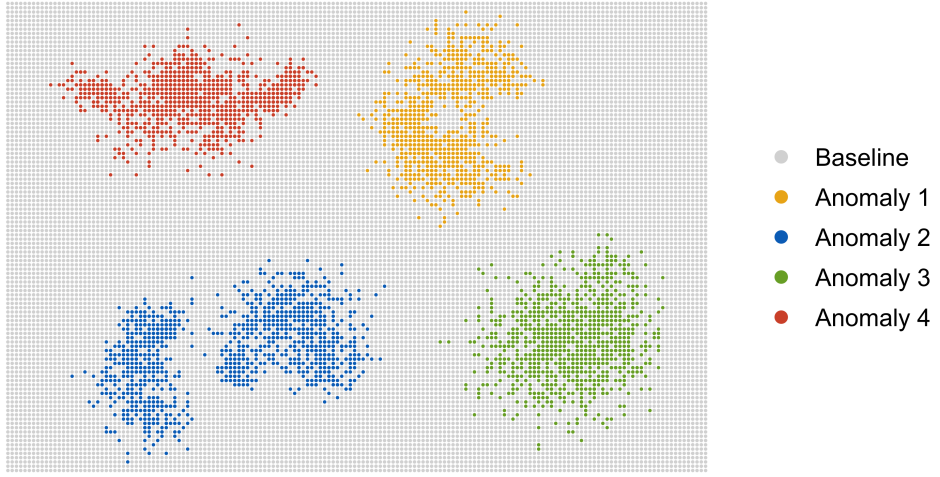


Figure 1: Illustration of spatial anomaly regions (each formed by a collection of points, highlighted in same colour) on a 2D spatial lattice, and the baseline region is plotted in grey points.

Next, we introduce some notations that will be used throughout this paper. For a spatial region R , we write $|R|$ as its cardinality, and denote $\bar{Y}_R = \frac{1}{|R|} \sum_{s \in R} Y(s)$ as the regional sample average. We denote $\bar{\mu}_R = \frac{1}{|R|} \sum_{s \in R} \mu(s)$ as the regional average of the mean signals. For two regions R and R' , we denote $R \setminus R' = R \setminus (R \cap R')$ as the region subtraction. When there is no ambiguity, we sometimes refer to the sets of regions $\{R_1, \dots, R_m\}$ and mean signals $\{\mu_1, \dots, \mu_m\}$ as $R_{1:m}$ and $\mu_{1:m}$, respectively. We denote the underlying true baseline and anomaly regions, and their mean signals as $\{R_0^*, R_{1:m^*}^*\}$ and $\{\mu_0^*, \mu_{1:m^*}^*\}$, and denote the estimated versions as $\{\hat{R}_0, \hat{R}_{1:\hat{m}}\}$ and $\{\hat{\mu}_0, \hat{\mu}_{1:\hat{m}}\}$, where m^* is the number of true anomalies and \hat{m} is its estimate.

2.2 Regional loss and penalised cost function

Consider a loss function $L(R; \mu)$, which measures the fit to data of a region R with a common mean signal μ . Often, appropriate losses are specified by parametrically modelling the data in the region, and then setting the loss to be some seminal measures, e.g., the negative of the log-likelihood or M -estimation, under such a model. Throughout this paper, we employ the least squares loss, which has been extensively used in the changepoint and anomaly detection literature (e.g., see Killick et al. (2012); Wang et al. (2020)). In this way,

$$L(R; \mu) := \frac{1}{\sigma^2} \sum_{s \in R} (Y(s) - \mu)^2.$$

Minimising over the mean signal μ implies

$$\bar{Y}_R = \hat{\mu}_R := \arg \min_{\mu} L(R; \mu).$$

Hence, we write the minimised loss in region R as $L(R) := L(R; \bar{Y}_R)$. Next, for a set of anomaly regions $R_{1:m}$, the baseline region is defined as $R_0 = \mathcal{S} \setminus \bigcup_{j=1}^m R_j$. As is common in the anomaly detection literature, we assume knowledge of the mean value μ_0^* and the variance proxy σ^2 throughout the rest of the paper. Otherwise, they can be obtained through robust procedures, for example, estimate μ_0^* using the median and estimate σ^2 using the median absolute deviation (MAD) approach (Fisch et al., 2022). As a result, we always write $L(R_0) = \sum_{s \in R} (Y(s) - \mu_0^*)^2 / \sigma^2$.

In a vast number of timeline changepoint/anomaly detection works (Yao, 1988; Zheng et al., 2022), the number and locations of anomalies are estimated by minimising the L_0 penalised cost

$$L(R_{1:m}) + \beta m, \quad (2.1)$$

where βm is a penalty with the tuning parameter β , and $L(R_{1:m}) := L(R_0) + \sum_{j=1}^m L(R_j)$ denotes the least squares loss of the partition $R_{1:m}$. However, in the context of spatial anomaly detection, minimising the penalised cost (2.1) does not yield a reliable estimate of m^* and $R_{1:m^*}^*$. For example, when two spatially distant anomaly regions exhibit similar mean signal levels, the minimiser of (2.1) fails to distinguish between them. Therefore, we propose an additional regional penalty, which punishes the “intrinsic area” of each anomaly region. To define such a penalty, we introduce the following concept of the minimum convex hull.

Definition 1. (*Minimum convex hull*) *The minimum convex hull of a region R is defined as the convex polygon with the fewest number of points in the lattice that encloses R , denoted by $Co(R)$.*

Figure 2 illustrates examples of the minimum convex hull. It efficiently captures the scatteredness of a region while its cardinality is not solely dependent on the number of points within the region. Figure 2(b) shows that the cardinality of the minimum convex hull could increase significantly if we add a few distant points to the original region.

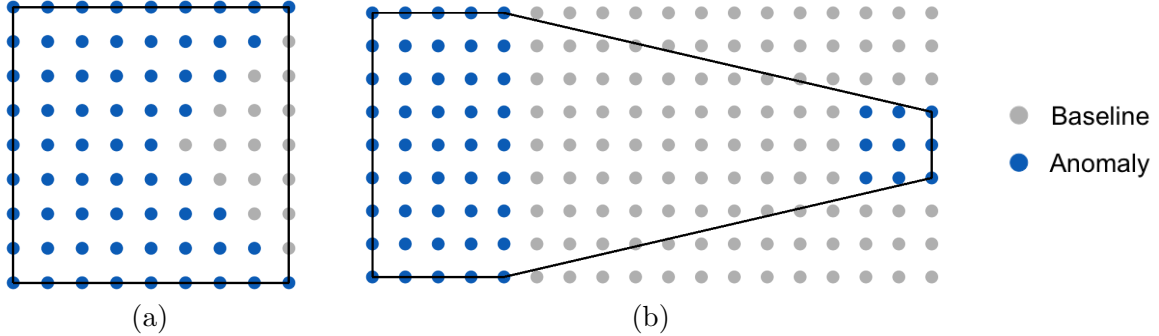


Figure 2: Minimum convex hull (points contained within the solid line) of anomaly regions. (a) The anomaly region is concave, and its minimum convex hull is a square that encloses all the anomaly points plus a few baseline points. (b) We added 9 distant points on the right side to the original anomaly region (whose minimum convex hull is a rectangular), the resulted new minimum convex hull encompasses many baseline points.

In this way, we estimate m^* and $R_{1:m^*}^*$ by minimising the following cost function, namely the double penalised least squares for spatial anomaly detection (DPLS-SAD):

$$C(m; R_{1:m}) := L(R_{1:m}) + \beta m + \lambda \sum_{j=1}^m |\text{Co}(R_j)|,$$

where both β and λ are penalty parameters. The L_0 penalty term βm has been well-studied in the literature, which avoids overestimation of anomaly numbers by imposing a penalty of β for each estimated anomaly region. The regional penalty, $\lambda \sum_{j=1}^m |\text{Co}(R_j)|$, serves to regularise the solution by discouraging the erroneous merging of spatially distant anomaly regions. The least squares loss, together with the two penalty terms, strikes a balance among model goodness of fit, parsimony in anomaly numbers, and the compactness of each anomaly.

3 Consistency theory

We establish theoretical guarantees for SAD, from which we want to estimate the number of anomalies and recover their regions on the lattice. Before proceeding to the main theorem, we first introduce some notations and technical assumptions.

Define the minimal anomaly region size and the minimal anomaly signal as

$$\delta := \min_{j=1,\dots,m^*} |R_j^*| \quad \text{and} \quad \Delta := \min_{j=1,\dots,m^*} |\mu_j^* - \mu_0^*|,$$

respectively. The definition of Δ ensures that the mean signal of each anomaly region is well separated from the baseline. We highlight that there is no restriction on the mean signal difference across different anomaly regions.

Define the intrinsic diameter of a region R as the largest pairwise distance between any two grid points in R :

$$r_R = \max_{\mathbf{s}, \mathbf{s}' \in R} \text{dist}(\mathbf{s}, \mathbf{s}'),$$

where $\text{dist}(\cdot, \cdot)$ denotes the Euclidean distance, which can be replaced by other well-defined distance metrics depending on the applications. We also define the distance between any two regions as the smallest Euclidean distance between any pair of grids from each region:

$$\text{dist}(R, R') = \min_{\mathbf{s} \in R, \mathbf{s}' \in R'} \text{dist}(\mathbf{s}, \mathbf{s}').$$

Analogous to classical timeline changepoint and anomaly detection frameworks, we impose the following assumptions to ensure the detectability of spatial anomaly regions. Specifically, we require sufficient signal distinguishability between anomaly and baseline regions, as well as adequate spatial separation between different anomalies.

Assumption 2. (Signal strength) (i) For any $\eta > 0$, there exists a constant $C_\eta > 0$, such that

$$\frac{\Delta^2}{\sigma^2} \geq C_\eta \cdot \frac{\log^{1+\eta} n}{\sqrt{n}}.$$

(ii) There exists a constant $0 < C_R < 1$, such that $\delta \geq C_R \cdot n$.

(iii) There exist $0 < d_A < d_B < 1$ such that the maximum intrinsic diameter of true anomaly regions, and the minimum distance between any two true anomaly regions satisfy:

$$\max_j r_{R_j^*} \leq d_A \sqrt{n} \quad \text{and} \quad \min_{i,j} \text{dist}(R_i^*, R_j^*) \geq d_B \sqrt{n}.$$

Assumption 2 (i) and (ii) ensure that the mean signal of the baseline and that of any anomaly region are distinct enough, and each anomaly region is sufficiently large. Altogether, they lead to a lower bound on the conventional signal-to-noise ratio (SNR) of detection, given by $\frac{\delta\Delta^2}{\sigma^2} \geq C_\eta \cdot \sqrt{n} \log^{1+\eta} n$. The SNR rate here is different from the $\log n$ rate in the timeline problem (Wang et al., 2020). In Section 4, we prove this cannot be relaxed to have any consistent detection. Assumption 2 (iii) requires that the anomaly regions are sufficiently separated from each other, with distances exceeding the intrinsic diameter of any anomaly region.

Remark 1. The well-separation assumption is essential when there exist different anomaly regions having similar or even the same mean values. If we require a stronger SNR condition, e.g., all the anomaly regions have different mean signals, then Assumption 2(iii) can be relaxed. We refer to the Supplementary Material A for an alternative set of assumptions and detailed discussions.

Next, we introduce a sub-class of “smooth” regions for follow-up theoretical analysis.

Definition 2. (Smooth regional class) Define the class of smooth regions as $\mathcal{R} = \mathcal{R}_K$, where $0 < K < \infty$ is a finite constant that does not depend on n and m^* , such that, at any fixed horizontal coordinate $1 \leq s_1 \leq n_1$, each region in \mathcal{R} can be divided into at most K consecutive segments (intervals).

Assumption 3. (Regional smoothness) (i) Each true anomaly region R_j^* belongs to the class of smooth regions, i.e., $R_j^* \in \mathcal{R}$ for $j \in \{1, \dots, m^*\}$.

(ii) There exists a constant $C_\delta > 0$ such that $|Co(R_j^*)| - |R_j^*| \leq C_\delta \cdot \delta$, $j = 1, \dots, m^*$.

Assumption 3(i) imposes a restriction on the geometry of the manifold formed by the points in each region. See Figure 3 for illustration. Equivalently, we can assume that, at any fixed vertical coordinate $1 \leq s_2 \leq n_2$, each true anomaly region can be divided into at most K segments. By limiting the number of consecutive segments at each horizontal or vertical direction, we rule out regions with too many holes, too many disconnected components, or extremely non-smooth boundaries. Note that the requirement is quite mild, under which we can still allow regions with at most $O(\sqrt{n})$ holes and disconnected components. Assumption 3(ii) limits the difference between each true anomaly region and its convex hull. Note that we allow their difference in cardinality to be as large as $O(n)$, which offers great flexibility in the shape of the region.

Our final estimator for the spatial anomaly detection is:

$$\{\hat{m}; \hat{R}_{1:\hat{m}}\} = \arg \min_{m; R_{1:m} \in \mathcal{R}} C(m; R_{1:m}), \quad (3.1)$$

where we restrict the minimisation within the smooth regional class \mathcal{R} from Definition 2. To measure the fitness of estimated anomalies compared to the true regions, we can use the symmetric regional difference, which measures the number of points that have been missed or falsely included in the detection:

$$D(R, R') := |R \setminus R'| + |R' \setminus R| = |R \cup R'| - |R \cap R'|.$$

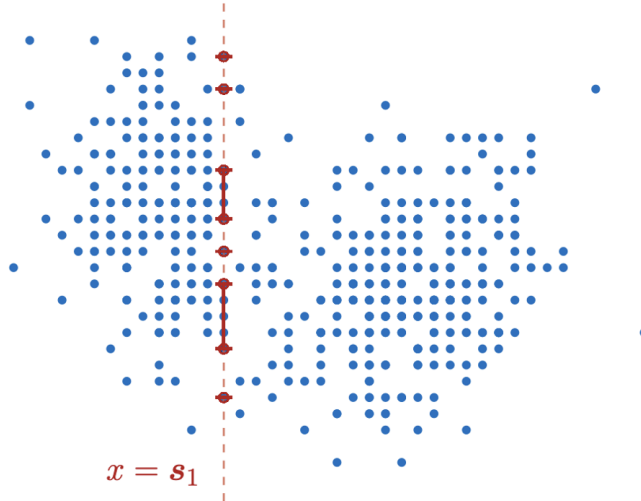


Figure 3: Illustration of the regional smoothness condition (i). At the same horizontal coordinate s_1 (grid points on the red line), the anomaly region can be divided into 6 segments, each is a collection of consecutive points on the line. Any isolated point is counted as a single segment.

This distance is equivalent to the Hausdorff-type localisation error $|s - s'| + |e - e'|$ in the timeline scenario, where (s, e) and (s', e') are pairs of starting and ending points of different intervals.

Now we are ready to present our main result in the following theorem, which shows that the number of anomalies and their locations can be consistently recovered by DPLS-SAD.

Theorem 1. (Consistency) *Suppose Assumptions 1, 2 and 3 hold. If we choose $\beta = C_\beta \sqrt{n} \log n$ and $\lambda = C_\lambda \log n / \sqrt{n}$, where C_β and C_λ are some absolute constants not depending on n and m^* . Let $\{\hat{m}; \hat{R}_{1:\hat{m}}\}$ be the minimiser from solving (3.1). There exist constants $c_\gamma, C_\varepsilon > 0$ such that*

$$\hat{m} = m^* \quad \text{and} \quad D\left(\hat{R}_j, R_j^*\right) \leq \frac{C_\varepsilon \sigma^2}{\Delta^2} \sqrt{n} \log n, \quad j = 1, \dots, m^*$$

holds with probability at least $1 - 2 \exp(-c_\gamma \sqrt{n} \log n)$.

Theorem 1 provides a non-asymptotic characterisation of DPLS-SAD detection. Such characterisation leads to straightforward consistent results for different asymptotic regimes. For example, consider the standard setup in the changepoint literature, where we have constant variance proxy σ^2 and jumping size Δ , we can see that the localisation error rate is $\sqrt{n} \log n$ with probability approaching 1, as $n \rightarrow \infty$.

Remark 2. Our detection result is similar to that in the classic timeline anomaly/changepoint detection problem (Fisch et al., 2022; Zheng et al., 2022), where the detection rate is $O(\log n)$. Here, DPLS-SAD obtains a different rate $O(\sqrt{n} \log n)$. The extra \sqrt{n} can be regarded as the price of transitioning from timeline to spatial detection. In Section 4, we further prove that this rate is minimax optimal up to a logarithmic factor and therefore cannot be further improved.

In view of Theorem 1, we allow great flexibility on the geometric shape of anomaly regions, as it is constrained solely by Assumptions 3. This makes the DPLS-SAD method practically useful in many real-world applications, where the shapes of anomalies are typically complex and irregular. It is worthwhile to note that there is a trade-off between the geometric flexibility of anomaly regions and the detection rate. Imposing excessive shape constraints will change the nature of the spatial detection problem. For example, assuming very strict convexity and connectivity restrictions on the anomaly regions makes the spatial detection problem a trivial extension of the timeline counterpart, thus leading to a similar localisation rate of $O(\log n)$.

In reality, sometimes anomaly regions are not spatially well-separated. We also consider a slightly different detection problem in Supplementary Material A, where we allow anomaly regions to be spatially close to each other, i.e., relaxing Assumption 2(iii). In such case, similar detection rate can be achieved under stronger SNR conditions.

4 Minimax optimal detection rate

In this section, we provide rigorous minimax arguments to analyse the spatial anomaly detection problem. We establish an SNR threshold below which consistent detection is impossible for any method. When the SNR exceeds this threshold, consistent detection becomes possible, and we provide an information-theoretic lower bound on the detection error rate. As a consequence, we also demonstrate that DPLS-SAD achieves the minimax rate-optimal detection up to a logarithm factor.

In Theorem 2 below, we give the impossible regime of consistent detection. In detail, suppose that the following low SNR condition holds

$$\frac{\delta\Delta^2}{\sigma^2} < \sqrt{n} \log n.$$

No consistent estimator of the spatial anomaly regions exists, e.g., for any detection method

we can always find some data scenario such that $\frac{\text{Detection error rate}}{n}$ is bounded away from 0.

Theorem 2. *(Impossible regime) Let \mathcal{Q} be a class of distributions satisfying the model setup in Section 2.1, and suppose Assumption 1 holds. As long as $\delta\Delta^2/\sigma^2 < \sqrt{n}\log n$, for sufficiently large n ,*

$$\inf_{\hat{R}} \sup_{Q \in \mathcal{Q}} \mathbb{E}_Q \left\{ D(\hat{R}, R(Q)) \right\} \geq \frac{n}{64},$$

where \hat{R} denotes the estimator of the set of anomaly regions, i.e., $\hat{R}_{1,\hat{m}}$; $R(Q)$ denotes the true anomaly regions under the distribution Q ; and the infimum is taken over all estimators.

In the impossible SNR regime, the minimax detection rate is $O(n)$, therefore the detection is never consistent. In the next theorem, we will show that when the SNR increases to the regime

$$\frac{\delta\Delta^2}{\sigma^2} \geq \sqrt{n}\log n,$$

the minimax detection rate can be improved to \sqrt{n} , which leads to consistent detection, i.e., $\frac{\text{Detection error rate}}{n} \rightarrow 0$ as $n \rightarrow \infty$.

Theorem 3. *(Minimax optimal rate) Let \mathcal{Q} be a class of distributions satisfying the model setup in Section 2.1, and suppose Assumption 1 holds. As long as $\delta\Delta^2/\sigma^2 \geq \sqrt{n}\log n$, for sufficiently large n , it holds that*

$$\inf_{\hat{R}} \sup_{Q \in \mathcal{Q}} \mathbb{E}_Q \left\{ D(\hat{R}, R(Q)) \right\} \geq \frac{\sigma^2}{2\Delta^2} \cdot \sqrt{n}.$$

From Theorems 2 and 3, we can see the minimax detection rate crucially depends on if SNR is less or greater than $\sqrt{n}\log n$. This is quite similar to the phase transition phenomenon observed in the timeline univariate change-in-mean problem (Verzelen et al., 2023; Wang and Samworth, 2018; Wang et al., 2020), where the minimax localisation rate is $O(n)$ in the low SNR regime ($\delta\Delta^2/\sigma^2 < \log n$) and improved to $O(1)$ in the high SNR regime ($\delta\Delta^2/\sigma^2 \geq \log n$).

Recall Theorem 1, in which we show DPLS-SAD achieves the detection error

$$D(\hat{R}_j, R_j^*) \leq \frac{C_\varepsilon \sigma^2}{\Delta^2} \sqrt{n} \log n.$$

This matches the minimax optimal rate up to a logarithm factor.

Remark 3. *It is worth pointing out that we employ a Fano-type argument to derive the minimax lower bounds in the proofs of Theorems 2 and 3, in contrast to the Le Cam's*

method commonly used in timeline problems. The Fano approach yields a sharp lower bound, whereas Le Cam’s method is insufficient in the spatial context. The construction and techniques developed in our proofs may also be of independent interest to the reader.

5 Extending to general dimensions and spatial dependent data

We now extend DPLS-SAD to detect anomaly regions in higher dimensions ($d > 2$), whilst each dimension is allowed to diverge at a different rate. Consistency and minimax results similar to those established in Sections 3 and 4 can be derived in this more general setting. Furthermore, we demonstrate that the independent data assumption can be relaxed, showing that our method remains valid for detecting anomaly regions under spatial dependence.

5.1 Anomaly detection for general dimensional data

Consider the process $\{Y(\mathbf{s}) : \mathbf{s} \in \mathcal{S}\}$, where $\mathcal{S} = \{(s_1, \dots, s_d)\} \subset \mathbb{R}^d$ is a set of points on a d -dimensional spatial lattice. Again we assume each $Y(\mathbf{s})$ can be decomposed into a mean signal and a random error:

$$Y(\mathbf{s}) = \mu(\mathbf{s}) + \varepsilon(\mathbf{s}), \quad \mathbf{s} \in \{1, 2, \dots, n_1\} \times \dots \times \{1, 2, \dots, n_d\},$$

where n_i is the size of i -th dimension, with $n = \prod_{i=1}^d n_i$. Define $n_{\max} = \max_i n_i$, which represents the maximum size of any dimension. Similar to Section 3, $\mu(\mathbf{s})$ denotes the common mean signal of the data in an anomaly region R if $\mathbf{s} \in R$.

Consider $\varepsilon(\mathbf{s})$ being sub-Gaussian as in Assumption 1. In the following, we update the Assumptions 2 (signal strength) and 3 (regional smoothness), respectively, to accommodate the general dimensionality.

Assumption 4. (i) For any $\eta > 0$, there exists a constant $C_\eta > 0$, such that

$$\frac{\Delta^2}{\sigma^2} \geq C_\eta \cdot \frac{\log^{1+\eta} n}{n_{\max}}.$$

(ii) Same as Assumption 2 (ii).

(iii) There exist $0 < 2d_A < d_B < 1$ such that the maximum intrinsic diameter of

anomaly regions and the minimum distance between two anomaly regions satisfy

$$\max_j r_{R_j^*} \leq d_A \cdot n_{\max} \quad \text{and} \quad \min_{i,j} \text{dist}(R_i^*, R_j^*) \geq d_B \cdot n_{\max}.$$

Assumption 4(iii) imposes a stronger spatial separation condition than Assumption 2(iii), requiring $d_B > 2d_A$, which means anomaly regions in general dimension must be considerably further apart from one another.

Definition 3. Define the class of d -dimensional smooth regions as $\mathcal{R}^d = \mathcal{R}_K^d$, where $0 < K < \infty$ is a finite constant that does not depend on n and m^* , such that for any axis-parallel line obtained by fixing $d - 1$ coordinates, the set of \mathcal{S} lying on this line can be partitioned into no more than K consecutive segments (intervals).

Assumption 5. (i) Each true anomaly region R_j^* , for $j \in \{1, \dots, m^*\}$, belongs to the class of d -dimensional smooth regions, that is, $R_j^* \in \mathcal{R}^d$ for all j .

(ii) Same as Assumption 3(ii).

In the DPLS-SAD methodology for general dimensional spatial data, we use the same double penalised cost and obtain the detected anomalies by minimising over \mathcal{R}^d , i.e.,

$$\{\hat{m}; \hat{R}_{1:\hat{m}}\} = \arg \min_{m; R_{1:m} \in \mathcal{R}^d} C(m; R_{1:m}). \quad (5.1)$$

The following theorem gives a consistency guarantee for the DPLS-SAD method in general dimensions.

Theorem 4. Suppose Assumptions 1, 4 and 5 hold. If we choose $\beta = C_{\beta,1} n \log n / n_{\max}$ and $\lambda = C_{\lambda,1} \log n / n_{\max}$, where $C_{\beta,1}$ and $C_{\lambda,1}$ are large enough absolute constants not depending on n and m^* . Let $\{\hat{m}; \hat{R}_{1:\hat{m}}\}$ be the minimiser from solving (5.1). There exist constants $c_{\gamma,1}, C_{\varepsilon,1} > 0$ such that

$$\hat{m} = m^* \quad \text{and} \quad D\left(\hat{R}_j, R_j^*\right) \leq \frac{C_{\varepsilon,1} \sigma^2}{\Delta^2} \cdot \frac{n}{n_{\max}} \log n, \quad j = 1, \dots, m^*$$

holds with probability at least $1 - 2 \exp\left(-c_{\gamma,1} \frac{n}{n_{\max}} \log n\right)$.

Remark 4. Theorem 4 shows the consistency result in general dimensional data, where the convergence rate is related to the maximum dimension size n_{\max} . When all the dimensions are of equal sizes, i.e., $n_1 = \dots = n_d = \sqrt[d-1]{n}$, the detection rate is $n^{\frac{d-1}{d}} \log n$. One can

observe the phenomenon of the curse of dimensionality, as the detection rate grows to n (meaning the problem is not detectable) as d increases to infinity.

Theorem 1 can be regarded as a special case of above result by setting $d = 2$ and $n_{\max} = \sqrt{n}$. In addition, setting $d = 1$ recovers the $\log n$ error rate in the timeline change-point/anomaly detection problem, in agreement with results established in the existing literature.

The following theorem extends the corresponding minimax results from the 2D problem to general dimensions, analogous to those in Section 4.

Theorem 5. *Let \mathcal{Q} be a class of distributions satisfying the model setup in Section 5.1, and suppose Assumption 1 holds. Then, for sufficiently large n ,*

$$\inf_{\widehat{R}} \sup_{Q \in \mathcal{Q}} \mathbb{E}_Q \left\{ D(\widehat{R}, R(Q)) \right\} \geq \begin{cases} \frac{n}{64}, & \text{if } \frac{\delta\Delta^2}{\sigma^2} < \frac{n}{n_{\max}} \log n, \\ \frac{\sigma^2}{2\Delta^2} \cdot \frac{n}{n_{\max}}, & \text{if } \frac{\delta\Delta^2}{\sigma^2} \geq \frac{n}{n_{\max}} \log n. \end{cases}$$

Similar to the results in Section 4, Theorem 5 reveals that the detection rate depends on if SNR is greater than the threshold $\frac{n}{n_{\max}} \log n$ or not. Combining with Theorem 4, DPLS-SAD achieves the minimax optimal detection rate, up to a logarithmic factor.

5.2 Anomaly detection for spatially dependent data

Previously, we assume the random errors $\{\varepsilon_s\}$ are independent to each other, which may not strictly hold in many real-world spatial applications. We now establish new results showing that DPLS-SAD still delivers consistent detection under certain spatial correlated data settings.

First, consider the following assumption on spatial dependence, which is the counterpart to Assumption 1.

Assumption 6. *Let $\varepsilon(\mathbf{s})$ be centered sub-Gaussian errors with $\|\varepsilon(\mathbf{s})\|_{\psi_2}^2 \leq \sigma^2$ for all $\mathbf{s} \in \mathcal{S}$. Moreover, for any $R \in \mathcal{R}^d$, assuming that*

$$\mathbb{E} \left\{ \exp \left(\tau \sum_{\mathbf{s} \in R} \varepsilon(\mathbf{s}) \right) \right\} \leq \exp (\tau^2 \sigma^2 |R|^\phi),$$

for all $\tau > 0$, where $\phi \geq 1$ is a dependence parameter satisfying $n^{\phi-1} \leq n_{\max}$.

Assumption 6 characterises the spatial dependence structure through the parameter ϕ . A larger value of ϕ corresponds to stronger positive dependence among data points. In particular, when $\phi = 1$, the data are assumed to be mutually independent.

The following theorem states that we can still achieve consistent detection by minimising the DPLS-SAD cost function as in (5.1).

Theorem 6. *Suppose Assumptions 4, 5 and 6 hold. If we choose $\beta = C_{\beta,2} \frac{n^\phi}{n_{\max}} \log n$ and $\lambda = C_{\lambda,2} \frac{n^{\phi-1}}{n_{\max}} \log n$, where $C_{\beta,2}$ and $C_{\lambda,2}$ are large enough absolute constants not depending on n and m^* . Let $\{\hat{m}; \hat{R}_{1:\hat{m}}\}$ be the minimiser from solving (5.1). There exist constants $c_{\gamma,2}, C_{\varepsilon,2} > 0$ such that*

$$\hat{m} = m^* \quad \text{and} \quad D\left(\hat{R}_j, R_j^*\right) \leq \frac{C_{\varepsilon,2}\sigma^2}{\Delta^2} \cdot \frac{n^\phi}{n_{\max}} \log n, \quad j = 1, \dots, m^*$$

holds with probability at least $1 - 2 \exp(-c_{\gamma,2} \frac{n}{n_{\max}} \log n)$.

Remark 5. Theorem 6 shows that the detection rate is related to the dependence parameter ϕ . When $\phi = 1$, which is corresponding to the data being independent, we attain the same $O\left(\frac{n}{n_{\max}} \log n\right)$ rate as in Theorem 4. Stronger spatial dependence (i.e., as ϕ increases) makes detection harder and leads to a larger localisation error bound.

Although we extend our framework to accommodate spatial dependence, in this paper we continue to employ the least squares cost function. A more appropriate choice for $L(R_{1:m})$ could be the negative full log-likelihood, which can explicitly model spatial dependence. However, this approach is typically intractable and computationally prohibitive. As an alternative, one may adopt the composite log-likelihood (Zhao et al., 2024). A detailed investigation of this extension is left for future work.

6 Algorithm for fast detection

We initially consider detecting spatial anomaly regions in 2D data, which requires numerically solving the optimisation problem (3.1). Classical changepoint algorithms, such as dynamic programming (Jackson et al., 2005; Killick et al., 2012) or pruning-based methods (Maidstone et al., 2017), are designed for sequential data, which are not applicable. The minimisation here is highly non-convex and NP-hard, making the problem computationally challenging, with a cost of $O(n^n)$. Therefore, we propose an efficient search strategy, inspired by one-dimensional k -means clustering algorithm (Wang and Song, 2011), that

computes an approximate instead of exact solution to (3.1), which reduces the computational cost to $O(n^4)$.

Consider a new sequence $\{Y_i\}_{i=1}^n$, with $|Y_1| \geq |Y_2| \geq \dots \geq |Y_n|$, as a rearrangement of $\{Y(\mathbf{s}) - \mu_0^*\}_{\mathbf{s} \in \mathcal{S}}$. In this way, all the baseline points are likely to be at the end of the new sequence. Denote \mathbf{s}_i as the corresponding lattice location of Y_i , and define $\mathcal{S}_{\mathcal{I}} = \{\mathbf{s}_i : i \in \mathcal{I}\}$ for some index set \mathcal{I} . Consider the following minimisation problem:

$$\min_{1 \leq N \leq n} \left[L(R_0^N) + \min_m \left\{ \min_{R_{1:m}^N} \left(\sum_{j=1}^m L(R_j^N) + \lambda \sum_{j=1}^m |\text{Co}(R_j^N)| \right) + \beta m \right\} \right], \quad (6.1)$$

where $R_{1:m}^N$ are m non-overlapping regions that form a segmentation of $\mathcal{S}_{1:N}$, i.e., $\bigcup_{j=1}^m R_j^N = \mathcal{S}_{1:N}$, and $R_0^N = \mathcal{S}_{N+1:n}$. The resulted minimiser gives an approximate solution to the original problem (3.1).

In problem (6.1), for fixed m and N , solving the minimisation over any segmentation $R_{1:m}^N$ on $\mathcal{S}_{1:N}$ is still not straightforward. Instead of obtaining $R_{1:m}^N$ through minimisation, we introduce the following Circular Region Segmentation (CRS) algorithm that provides a reasonable estimate efficiently by exploiting the spatial information of anomaly regions.

Algorithm 1 Circular Region Segmentation (CRS)

Input: $(Y_{1:N}, m, \xi)$, $\mathcal{N} = \{1, \dots, N\}$

```

1: for  $k = 1, \dots, m$  do
2:   Pick  $i = \min \mathcal{N}$ ;
3:   Calculate  $\tilde{R}_k^N = \mathcal{S}_{\mathcal{N}} \cap \mathcal{B}(\mathbf{s}_i, \sqrt{\frac{n}{m\pi}})$ 
4:   Update  $\mathcal{N} = \mathcal{N} \setminus \{j : \mathbf{s}_j \in \tilde{R}_k^N\}$ 
5:   if  $|\tilde{R}_k^N| \geq \xi$  then
6:      $k = k + 1$ 
7:   end if
8: end for

```

Output: $\tilde{R}_{1:m}^N$

In the Algorithm 1, $\mathcal{B}(\mathbf{s}, r)$ denotes a spatial ball on \mathcal{S} centered at \mathbf{s} with radius r , and ξ is a pre-defined threshold on the size of anomaly regions. Recall in Assumption 2(ii) and (iii), we require that anomaly regions are large enough and well-separated (distant from each other). Inspired by this assumption, in each iteration we divide the remaining points into a circular region and restrict their sizes to be no larger than n/m . We then intersect each of them with candidate grid points to approximate an anomaly. If additional information about the anomaly regions is available, the shape of $\mathcal{B}(\mathbf{s}, r)$ can be adapted,

for example, by using an ellipse or rectangle instead of a ball.

From Algorithm 1, we obtain a reasonable $\tilde{R}_{1:m}^N$ without solving the minimisation problem over all possible segmentations. The rest of points are all considered as baseline, denoted by \tilde{R}_0^N . Next, we only need to search over combinations of (m, N) , to find the best $\tilde{R}_{1:m}^N$ that minimises the following cost:

$$C(m, N) = \min_{1 \leq N \leq n} \left[L(\tilde{R}_0^N) + \min_m \left\{ \sum_{j=1}^m L(\tilde{R}_j^N) + \lambda \sum_{j=1}^m |\text{Co}(\tilde{R}_j^N)| + \beta m \right\} \right].$$

In this way, we propose our algorithm for DPLS-SAD below:

Algorithm 2 Approximated Double Penalised Least Squares for Spatial Anomaly Detection (DPLS-SAD)

Input: $(Y_{1:n}, \beta, \lambda)$,

```

1: for  $N = 1, \dots, n$  do
2:   for  $m = 1, \dots, N$  do
3:      $\tilde{R}_{1:m}^N = \text{CRS}(Y_{1:N}, m, \xi_m);$ 
4:     Calculate
5:      $\tilde{R}_0^N = \mathcal{S} \setminus \cup_{j=1}^m \tilde{R}_j^N$ 
6:      $C(m, N) = L(\tilde{R}_0^N) + \sum_{j=1}^m L(\tilde{R}_j^N) + \lambda \sum_{j=1}^m |\text{Co}(\tilde{R}_j^N)| + \beta m$ 
7:   end for
8: end for
9:  $(\tilde{m}, \tilde{N}) = \arg \min_{1 \leq m \leq n, 1 \leq N \leq n} C(m, N)$ 
```

Output: $(\tilde{m}, \tilde{R}_{1:\tilde{m}}^{\tilde{N}})$

Algorithm 2 provides an approximation to the estimates of the number and locations of anomaly regions through solving (3.1). The computational cost is $O(n^4)$, as the evaluation runs over N and m , and CRS has a quadratic runtime in N for each fixed N and m . If we have some prior information on m^* , the computational cost decreases accordingly. For example, when an upper bound of m^* is known as a constant, the overall complexity drops to $O(n^3)$. Algorithm 2 can be easily extended to higher dimensions, by changing $\mathcal{B}(\mathbf{s}, r)$ to a d -dimensional ball and setting the radius $r = \sqrt[d]{\frac{n\Gamma(d/2+1)}{m(\pi)^{d/2}}}$ in the CRS algorithm, where $\Gamma(\cdot)$ is the gamma function.

7 Simulation studies

In this section, we assess the empirical performance of DPLS-SAD and the proposed algorithm. To the best of our knowledge, most existing algorithms, such as those in image segmentation and clustering, are not well suited to the SAD problem. These methods typically ignore spatial distance and often impose convexity constraints on regions, which we find usually lead to very unreliable detection performance. In our experiments, we include DCART (Madrid Padilla et al., 2021) as a benchmark method, while noting that it is also not originally designed for the SAD setting.

For the data generating process, we set the random errors $\varepsilon(\mathbf{s})$ to be identically distributed $N(0, 1)$ random variables. As shown in Figure 4, three different settings of anomaly regions are considered: 1) five equal-sized square anomalies; 2) a ellipse anomaly, a circular anomaly with holes, and a disconnected anomaly; 3) a concave anomaly and a disconnected anomaly. We jitter the boundaries of anomaly regions in Settings 2 and 3, to make them less artificial. The baseline mean signal μ_0^* is fixed to be 0. Multiple combinations of signal-to-noise ratio, through changing the minimum anomaly mean signal Δ and the total area of anomalies $|R| = \sum_{j=1}^{m^*} |R_j^*|$, together with different sample sizes n are studied in our simulations.

We adopt two indicators to evaluate the performance of anomaly detection:

$$\text{NoC} = \frac{1}{B} \sum_{b=1}^B \mathbb{I}\{\hat{m}^b = m^*\} \quad \text{and} \quad \text{Err} = \frac{1}{B} \sum_{b=1}^B \text{Err}\left(R_{1:m^*}^*, \hat{R}_{1:\hat{m}^b}^b\right),$$

namely the frequency that we detect the correct number of anomalies and the averaged detection error, within B times of Monte Carlo simulations, where $\{\hat{m}^b; \hat{R}_{1:\hat{m}^b}^b\}$ denotes the detected anomalies in b -th simulation. The term $\text{Err}\left(R_{1:m^*}^*, \hat{R}_{1:\hat{m}}\right)$ consists of the sum of two error components adjusted by the total area of anomalies:

$$\text{Err}\left(R_{1:m^*}^*, \hat{R}_{1:\hat{m}}\right) = \frac{\sum_{i=1}^{\hat{m}} \min_{j=1, \dots, m^*} |\hat{R}_i \setminus R_j^*| + \sum_{j=1}^{m^*} \min_{i=1, \dots, \hat{m}} |R_j^* \setminus \hat{R}_i|}{|R|}.$$

The first component measures the error that points in an estimated anomaly do not overlap with the corresponding correct true anomaly region, and the second component measures the error that points in a true anomaly region that have not been detected correctly.

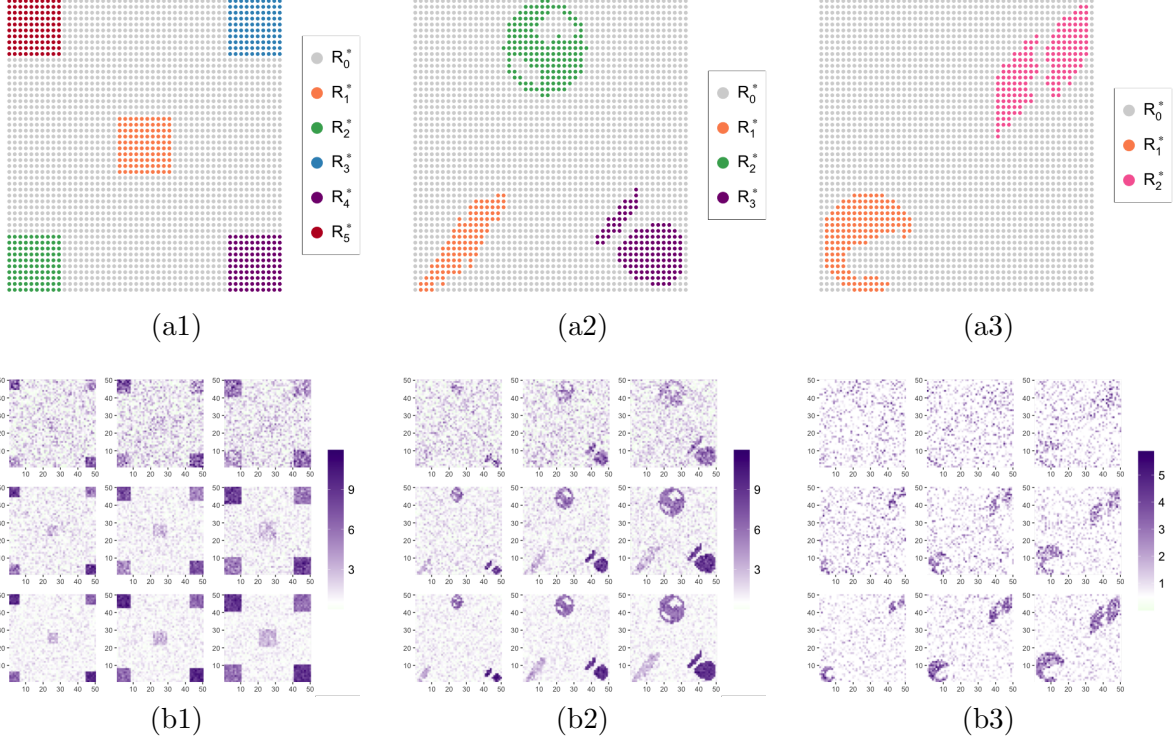


Figure 4: Plots of anomaly regions in three different settings (top panel) and realisations of the observed data under different combinations of Δ and $|R|$ (bottom panel), with sample size $n = 2500$. (a1) Setting 1: five square anomaly regions, where $\mu_1^* = \Delta$, $\mu_2^* = \mu_3^* = 2\Delta$, and $\mu_4^* = \mu_5^* = 3\Delta$; (a2) Setting 2: a ellipse anomaly, a circular anomaly with holes, and a disconnected anomaly, where $\mu_1^* = \Delta$, $\mu_2^* = 2\Delta$, and $\mu_3^* = 3\Delta$. (a3) Setting 3: a concave anomaly and a disconnected anomaly, where $\mu_1^* = \mu_2^* = \Delta$. (b1)-(b3): one time data realisation under different Δ and $|R|$ (top to bottom, Δ increasing; left to right, $|R|$ increasing.)

7.1 Simulation for independent data

We carry out $B = 100$ simulations under all three settings and different SNR combinations, with sample sizes $n = 400$ and $n = 2500$. We also assess $n = 1225$, which is deferred to the Supplementary Material.

We observe that the performance of DPLS-SAD is robust to a wide range of penalty parameter values (β, λ) . In theory, we require $\beta < |R_j^*| \cdot (\mu_j^* - \mu_0^*)^2$ to ensure a region is estimated as an anomaly only if doing so results in a sufficient reduction in regional loss. As a result, in most settings, we set $\beta = \Delta \cdot \delta$. From our theorems, λ is smaller than β roughly by a factor of n . Therefore, we fix $\lambda = \beta/n$ in the simulations. In practice, when (Δ, δ) are not available, we can select β based on sensitivity analysis. In the DPLS-SAD

algorithm, we always set the threshold as $\xi_m = 20 \cdot \lfloor \log_{10}(\sqrt{n}) \rfloor / m$, where m is the index of the inner loop iteration. Our results are summarised in Table 1 and Figure 5, where we also compare with DCART.

Note that DCART first partitions the lattice into multiple non-overlapping rectangles and then merges partitions with similar mean values to form anomaly regions. This approach tends to perform poorly in settings with complex-shaped anomalies (e.g., our Settings 2 and 3), where a large number of partitions is required to achieve accurate estimation. Furthermore, DCART struggles to distinguish between anomalies with similar mean signal values, whereas DPLS-SAD is capable of accurately separating them.

From Table 1, we can see that DCART only delivers reasonable results in Setting 1 under a few low SNR regimes. It is uniformly outperformed by DPLS-SAD, especially under non-regular anomaly settings, where the DCART often fails to detect any anomalies. The results also reveal that DPLS-SAD becomes more accurate as the mean signal and overall area of anomalies increase, which matches with our theoretical results in Section 3.

		n = 400						n = 2500													
		Setting 1			Setting 2			Setting 3			Setting 1			Setting 2			Setting 3				
		Δ	$ R $	45	80	125	29	43	60	18	26	42	180	320	500	99	228	401	82	177	313
DPLS-SAD	1	11	28	41	18	24	26	5	16	32	37	44	63	19	25	48	9	14	24		
	2	26	54	80	31	34	52	25	54	78	59	87	97	37	68	86	68	85	92		
	3	80	94	99	88	89	96	55	88	99	98	98	100	96	100	100	99	100	100		
NoC(%)	1	31	20	15	—	—	—	—	—	—	29	17	4	11	39	40	—	—	—		
	2	29	34	13	15	18	42	—	—	—	20	30	14	20	21	42	—	25	10		
	3	31	33	33	12	8	19	—	22	33	35	25	10	51	44	56	23	32	31		
DPLS-SAD	1	75	54	49	114	82	69	247	191	132	67	63	61	82	73	63	126	107	100		
	2	24	19	17	54	35	30	159	97	71	24	22	20	38	33	25	86	78	73		
	3	10	8	8	20	17	13	80	41	33	12	11	10	19	17	14	45	39	37		
Err(%)	1	48	41	44	—	—	—	—	—	—	41	50	56	103	89	73	—	—	—		
	2	37	33	40	111	94	70	—	—	—	29	35	40	72	60	49	—	103	96		
	3	25	25	31	87	72	58	—	95	98	26	32	40	54	50	43	127	98	74		

Table 1: Performances of DPLS-SAD and DCART, where “—” denotes that DCART estimates all the points as baseline in more than 95% simulations. In Settings 3, we scale both β and λ by factors of 0.65.

Figure 5 visualises the frequency that each spatial grid point is identified as an anomaly point within 100 simulations. The results demonstrate that DPLS-SAD successfully detects

anomaly regions even in challenging settings, including cases with complicated anomaly region shapes, and distinct regions sharing identical mean values.

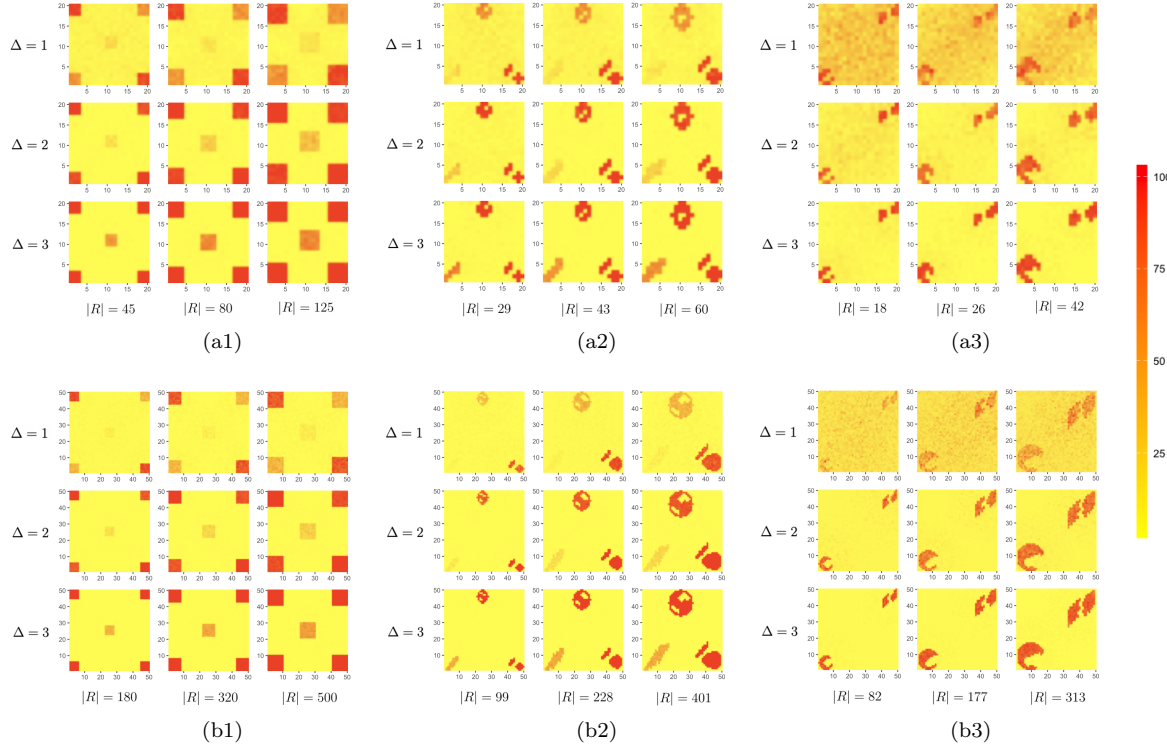


Figure 5: Frequency of points detected as anomalies, varying by 3 settings, with sample sizes $n = 400$ (top panel) and $n = 2500$ (bottom panel). Each setting and sample size includes 9 combinations of Δ and $|R|$ (top to bottom, Δ increasing; left to right, $|R|$ increasing).

7.2 Simulation for 2D dependent and 3D data

We extend our experiments to dependent spatial data and 3-dimensional settings. To generate 2D dependent data, we set the covariance between errors $\varepsilon(\mathbf{s})$ and $\varepsilon(\mathbf{s}')$ to be $\exp\{-\zeta \cdot \text{dist}(\mathbf{s}, \mathbf{s}')\}$ for any \mathbf{s} and \mathbf{s}' , where we consider different dependencies by taking $\zeta \in \{0.01, 0.5, 3\}$. Here we only examine data from Setting 2 with $n = 2500$, under varying values of Δ . For 3D data, we simulate two anomaly regions with the same mean signal Δ on a $12 \times 12 \times 12$ lattice, as shown in Figure 6 below.

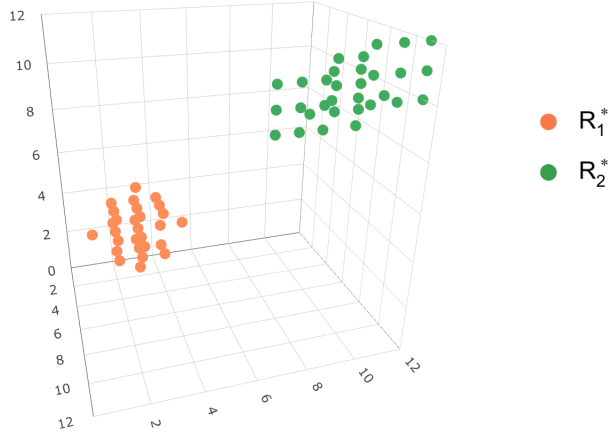


Figure 6: Plot of anomaly regions in three-dimensional data setting, where R_1 is a circular anomaly with holes, and R_2 is a disconnected anomaly, both have jittered points on the boundary. The baseline data points are not plotted.

We adopt the same parameter choices as in Section 7.1, where the L_0 penalty and regional penalty parameters are set to $\beta = \Delta \cdot \delta$ and $\lambda = \beta/n$, respectively. Our results are summarised in Table 2 and Figure 7. Note that other methods cannot handle dependent or 3D spatial data, hence we only present results from DPLS-SAD. It can be seen that the proposed method becomes more accurate as the signal strength Δ increases. Additionally, Table 2 and Figure 7 (a) indicate that a weaker dependence relationship (i.e., larger ζ) leads to better detection outcome, which is consistent with our theory.

	2D dependent data						3D data	
	NoC(%)			Err(%)			NoC(%)	Err(%)
	$\zeta = 0.01$	$\zeta = 0.5$	$\zeta = 3$	$\zeta = 0.01$	$\zeta = 0.5$	$\zeta = 3$		
$\Delta = 1$	21	23	27	134	75	73	15	133
$\Delta = 2$	52	53	66	39	33	33	52	92
$\Delta = 3$	75	85	100	19	18	17	92	48

Table 2: Performance of DPLS-SAD for 2D dependent and 3D data. Results are based on 100 Monte Carlo simulations, where we fix $|R| = 228$ for 2D dependent data and $|R| = 59$ for 3D data.

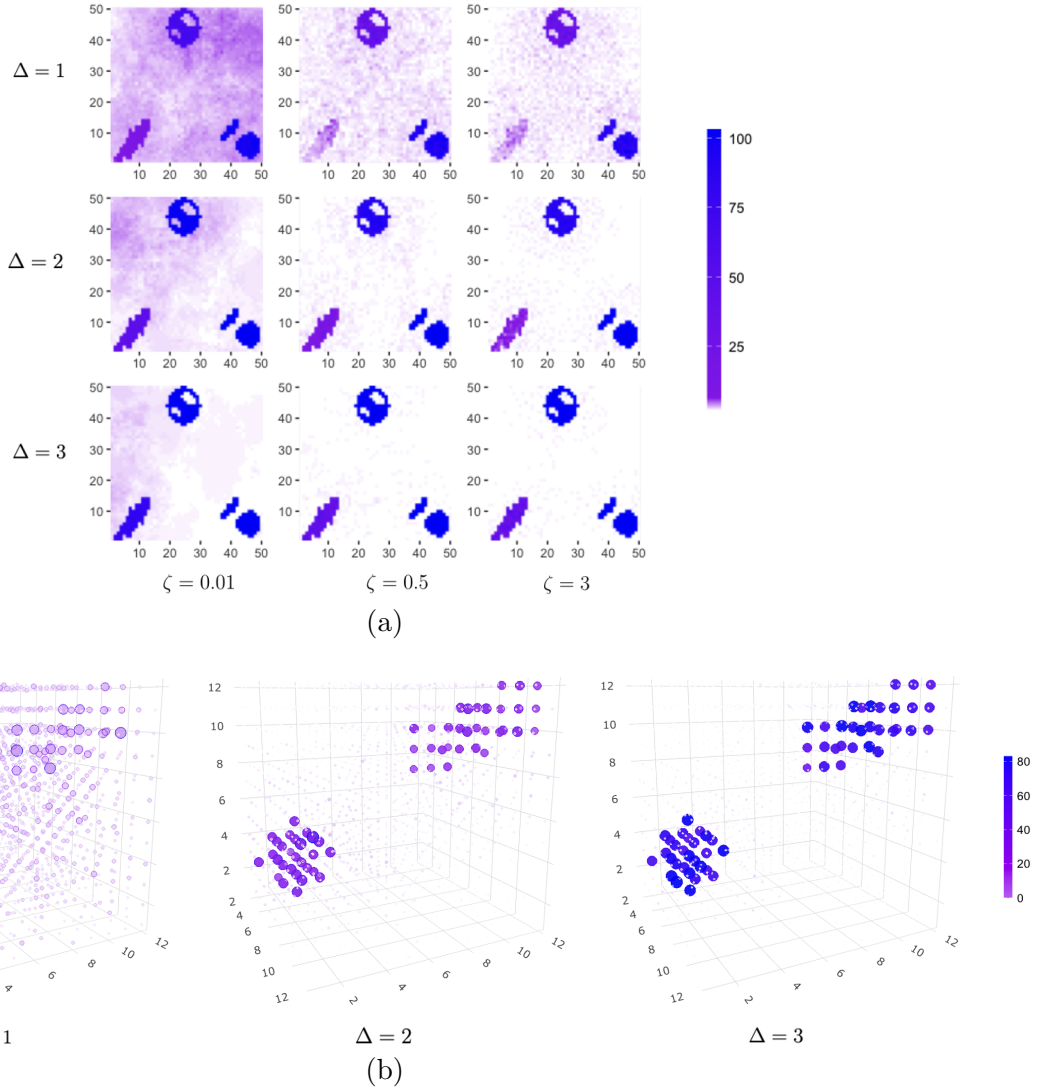


Figure 7: Frequency of points detected as anomalies for (a) 2D dependent data, and (b) 3D data. For 2D dependent data, we include 9 combinations of Δ and ζ (top to bottom, Δ increasing; left to right, ζ increasing); Bottom panel show the results for 3D data, varying among Δ (left to right, Δ increasing).

8 Real-world data application

We illustrate the proposed method by detecting marine heatwaves (MHWs) over the entire globe. Marine heatwaves have devastating impacts on marine ecosystems, including mass coral bleaching, substantial losses in kelp forests and seagrass, and declines in economically important species such as lobsters, crabs, abalones, and scallops (Holbrook et al., 2020). The importance of this research was amplified by anthropogenic warming, which

has doubled the occurrence of MHWs since 1982 and increased the total number of days with MHWs by 50% over the last century (Oliver et al., 2018). DPLS-SAD can provide an automatic identification of MHWs, whilst in existing literatures these events are usually specified manually by oceanographers.

To carry out our analysis of MHWs, we use the level-4 sea surface temperature (SST) data from the European Space Agency Climate Change Initiative (ESA-CCI) Programme, which provides global and gridded daily mean SST since 1980, derived from combining multiple series of thermal infra-red sensors (Embrey et al., 2024). We take a coarser version of the SST data with a grid resolution of 1° in longitude and latitude, which equates to a 360×180 spatial lattice. Only grid points located in the ocean are retained, resulting in a sample size of 42827.

A common linear yearly detrending is applied on each grid to eliminate seasonal variability and remove the anthropogenic warming trend. As the MHWs are more commonly studied in tropical and temperate regions, we restrict our analysis to latitudes between 55 degree south and 50 degree north. Given that MHWs usually persist for many weeks or months, we then take the maximum monthly average of the detrended SST between the years 2000 and 2023 over the spatial lattice. Figure 8 below provides a visualisation of our final pre-processed data, based on which we aim to simultaneously detect the major MHWs since the 21st century.

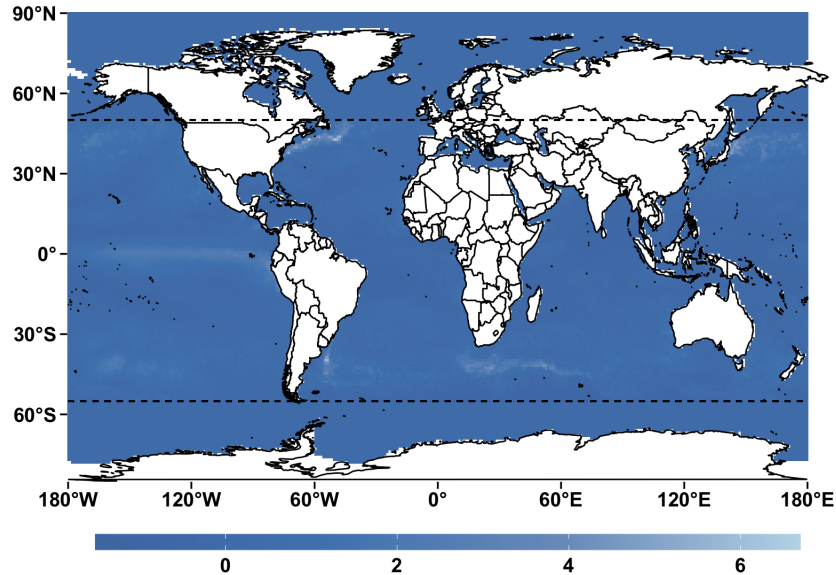


Figure 8: Maximum monthly detrended average SST across 2000–2023 (Land temperature are omitted). Lighter colours indicate higher SST.

For the selection of the tuning parameters, we perform a sensitivity analysis on a grid of L_0 penalty parameter β based on the scale of $\sqrt{n} \log n$, which indicates that choosing β between 450 and 550 yields both stable and reasonable MHW detections. Therefore, we set $\beta = 495$ and $\lambda = \beta/n$. To estimate the mean signal in the baseline region, DPLS-SAD was performed twice, and we update the baseline mean estimate in the second run using the median of the SST values of the detected baseline region from the first run.

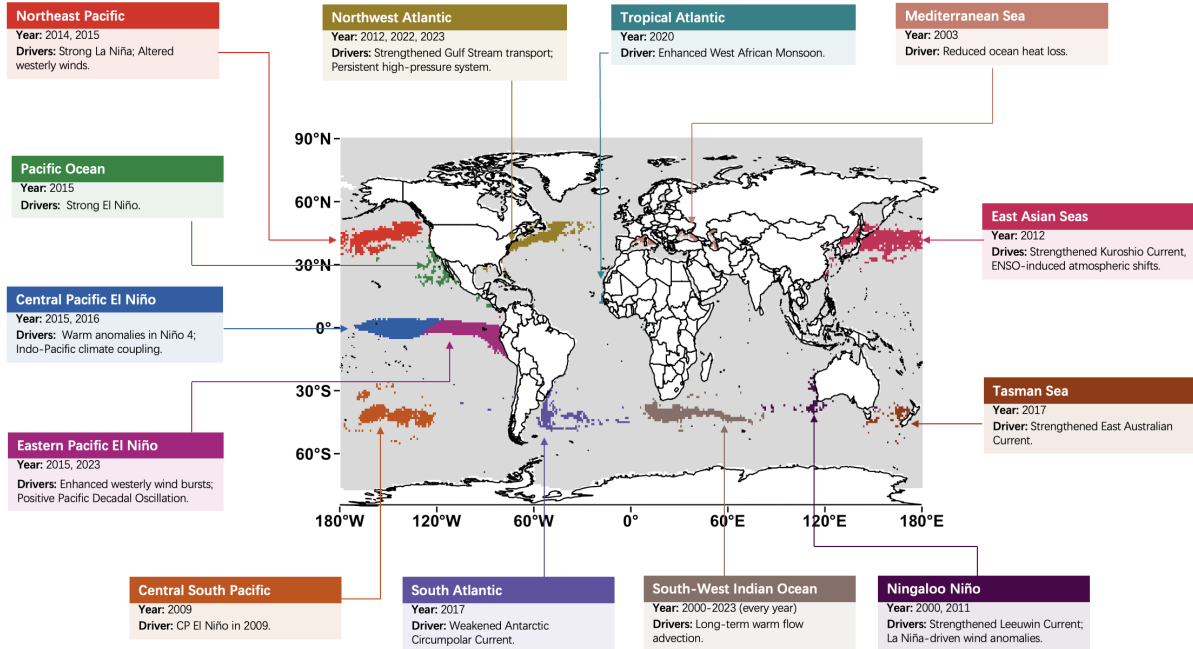


Figure 9: Anomaly regions are shown in different colors, with labels marking the active years and drivers of the corresponding MHW events. Detected anomalies are matched with historical major MHWs (with primary peak year and drivers) since 2000, including Northwest Atlantic (Mills et al., 2013; von Schuckmann et al., 2024), South Atlantic (Manta et al., 2018), East Asian Sea (Miyama et al., 2021), Central and Eastern El Niño (L’Heureux et al., 2017; Lian et al., 2023), Pacific Ocean (Fewings and Brown, 2019), Mediterranean Sea (Olita et al., 2007), Tropical Atlantic (Pfleiderer et al., 2022), Central South Pacific (Lee et al., 2010), Ningaloo Niño (Holbrook et al., 2020; Marshall et al., 2015), Northeast Pacific Ocean (Cavole et al., 2016), Tasman Sea (Kajtar et al., 2022).

In Figure 9, we demonstrate the result of applying DPLS-SAD to the pre-processed data, compared to the historical MHW records. Our method provides a highly accurate and reliable detection of major MHWs hotspots since 2000 (Oliver et al., 2021), recovering their complex shapes. The only exception is the active warm zone in the Southwest Indian Ocean, which is not linked to specific MHW events. However, the area stays warm frequently due to long-term ocean processes like the Agulhas Current and warm eddies, which bring heat

from the Indian Ocean into the South Atlantic (Beal et al., 2011). It is interesting to note that we automatically segment the significant MHWs in the Pacific Ocean caused by El Niño into two nearby anomaly regions. The central Pacific region, linked to CP-type El Niño events in 2015 and 2016, is affected by atmospheric changes and shows stronger connections with the southern Indian Ocean. While the eastern Pacific region is linked to EP-type El Niño, which was active in 2015 and 2023, and mainly driven by large-scale changes in the thermocline and surface winds that are closely related to the tropical Indian Ocean (Kao and Yu, 2009).

References

Beal, L. M., De Ruijter, W. P., Biastoch, A. and Zahn, R. (2011) On the role of the Agulhas system in ocean circulation and climate. *Nature*, **472**, 429–436.

Boykov, Y., and Funka-Lea, G. (2006) Graph cuts and efficient ND image segmentation. *International Journal of Computer Vision*, **70**, 109–131.

Cavole, L. M., Demko, A. M., Diner, R. E., Giddings, A., Koester, I., Pagniello, C. M. L. S., Paulsen, M.-L., Ramirez-Valdez, A., Schwenck, S. M., Yen, N. K., Zill, M. E., and Franks, P. J. S. (2016) Biological impacts of the 2013–2015 warm-water anomaly in the Northeast Pacific: Winners, losers, and the future. *Oceanography*, **29**, 273–285.

Chan, N. H., Zhang, R., and Yau, C. Y. (2022) Inference for structural breaks in spatial models. *Statistica Sinica*, **32**, 1961–1981.

Chapman, C. C., Monselesan, D. P., Risbey, J. S., Feng, M., and Sloyan, B. M. (2022) A large-scale view of marine heatwaves revealed by archetype analysis. *Nature Communications*, **13**, 7843.

Cho, H. and Fryzlewicz, P. (2015) Multiple-change-point detection for high dimensional time series via sparsified binary segmentation. *Journal of the Royal Statistical Society Series B: Statistical Methodology*, **77**, 475–507.

Embry, O., Merchant, C. J., Good, S. A., Rayner, N. A., Hoyer, J. L., Atkinson, C., Block, T., Alerskans, E., Pearson, K. J., Worsfold, M., McCarroll, N. and Donlon, C. (2024) Satellite-based time-series of sea-surface temperature since 1980 for climate applications. *Scientific Data*, **11**, 326.

Fewings, M. R. and Brown, K. S. (2019) Regional structure in the marine heat wave of summer 2015 off the western United States. *Frontiers in Marine Science*, **6**, 564.

Fisch, A. T., Eckley, I. A. and Fearnhead, P. (2022) A linear time method for the detection of collective and point anomalies. *Statistical Analysis and Data Mining: ASA Data Science Journal*, **15**, 494–508.

Fodor, G., and Conde, M. V. (2023). Rapid deforestation and burned area detection using deep multimodal learning on satellite imagery. *Preprint arXiv:2307.04916*.

Fryzlewicz, P. (2014) Wild binary segmentation for multiple change-point detection. *Annals of Statistics*, **42**, 2243–2281.

Gromenko, O., Kokoszka, P. and Reimherr, M. (2017) Detection of change in the spatiotemporal mean function. *Journal of the Royal Statistical Society Series B: Statistical Methodology*, **79**, 29–50.

Gu, Q., Meroueh, C., Levernier, J., Kroneman, T., Flotte, T., and Hart, S. (2023) Using an anomaly detection approach for the segmentation of colorectal cancer tumors in whole slide images. *Journal of Pathology Informatics*, **14**, 100336.

Hansen, S., Gautam, S., Jenssen, R., and Kampffmeyer, M. (2022) Anomaly detection-inspired few-shot medical image segmentation through self-supervision with supervoxels. *Medical Image Analysis*, **78**, 102385.

Holbrook, N. J., Sen Gupta, A., Oliver, E. C. J., Hobday, A. J., Benthuysen, J. A., Scannell, H. A., Smale, D. A. and Wernberg, T. (2020) Keeping pace with marine heatwaves. *Nature Reviews Earth and Environment*, **1**, 482–493.

Jackson, B., Scargle, J. D., Barnes, D., Arabhi, S., Alt, A., Gioumousis, P., Gwin, E., Sangtrakulcharoen, P., Tan, L. and Tsai, T. T. (2005) An algorithm for optimal partitioning of data on an interval. *IEEE Transactions on Signal Processing Letters*, **12**, 105–108.

Kajtar, J. B., Bachman, S. D., Holbrook, N. J. and Pilo, G. S. (2022) Drivers, dynamics, and persistence of the 2017/2018 Tasman Sea marine heatwave. *Journal of Geophysical Research: Oceans*, **127**, e2022JC018931.

Kalantari, M., Ghezelbash, S., Ghezelbash, R., and Yaghmaei, B. (2020). Developing a fractal model for spatial mapping of crime hotspots. *European Journal on Criminal Policy and Research*, **26**, 571–591.

Kao, H. Y. and Yu, J. Y. (2009) Contrasting eastern-Pacific and central-Pacific types of ENSO. *Journal of Climate*, **22**, 615–632.

Killick, R., Fearnhead, P. and Eckley, I. A. (2012) Optimal detection of changepoints with a linear computational cost. *Journal of the American Statistical Association*, **107**, 1590–1598.

Kirch, C., Klein, P. and Meyer, M. (2025) Scan statistics for the detection of anomalies in M-dependent random fields with applications to image data. *Journal of the American Statistical Association*, (2025): 1-20.

Kovács, S., Bühlmann, P., Li, H., and Munk, A. (2023) Seeded binary segmentation: a general methodology for fast and optimal changepoint detection. *Biometrika*, **110**, 249–256.

Kulldorff, M. (1997) A spatial scan statistic. *Communications in Statistics-Theory and Methods*, **26**, 1481–1496.

Lee, T., Hobbs, W. R., Willis, J. K., Halkides, D., Fukumori, I., Armstrong, E. M., Hayashi, A. K., Liu, W. T., Patzert, W., and Wang, O. (2010) Record warming in the South Pacific and western Antarctica associated with the strong central-Pacific El Niño in 2009–10. *Geophysical Research Letters*, **37**.

L'Heureux, M. L., Takahashi, K., Watkins, A. B., Barnston, A. G., Becker, E. J., Di Liberto, T. E., Gamble, F., Gottschalck, J., Halpert, M. S., Huang, B., Mosquera Vásquez, K. A., and Wittenberg, A. T. (2017) Observing and predicting the 2015/16 El Niño. *Bulletin of the American Meteorological Society*, **98**, 1363–1382.

Li, X. Z., Wang, J. F., Yang, W. Z., Li, Z. J., and Lai, S. J. (2011) A spatial scan statistic for multiple clusters. *Mathematical Biosciences*, **233**, 135–142.

Lian, T., Wang, J., Chen, D., Liu, T., and Wang, D. (2023) A strong 2023/24 El Niño is staged by tropical Pacific Ocean heat content buildup. *Ocean-Land-Atmosphere Research*, **2**, 0011.

Madrid Padilla, O. H., Yu, Y., and Rinaldo, A. (2021) Lattice partition recovery with dyadic CART. *Advances in Neural Information Processing Systems*, **34**, pp. 26143–26155.

Maidstone, R., Hocking, T., Rigaill, G., and Fearnhead, P. (2017) On optimal multiple changepoint algorithms for large data. *Statistics and Computing*, **27**, 519–533.

Manta, G., de Mello, S., Trinchin, R., Badagian, J., and Barreiro, M. (2018) The 2017 record marine heatwave in the southwestern Atlantic shelf. *Geophysical Research Letters*, **45**, 12,449–12,456.

Marshall, A. G., Hendon, H. H., Feng, M., and Schiller, A. (2015) Initiation and amplification of the Ningaloo Niño. *Climate Dynamics*, **45**, 2367–2385.

Mills, K. E., Pershing, A., Brown, C. J., Chen, Y., Chiang, F.-S., Holland, D. S., Lehuta, S., Nye, J. A., Sun, J. C., Thomas, A. C. and Wahle, R. A. (2013) Fisheries management in a changing climate: lessons from the 2012 ocean heat wave in the Northwest Atlantic. *Oceanography*, **26**, 191–195.

Miyama, T., Minobe, S. and Goto, H. (2021) Marine heatwave of sea surface temperature of the Oyashio region in summer in 2010–2016. *Frontiers in Marine Science*, **7**, 576240.

Moore, A., Chu, L., and Zhu, Z. (2025). Adaptive Block-Based Change-Point Detection for Sparse Spatially Clustered Data with Applications in Remote Sensing Imaging. *Preprint arXiv:2505.21814*.

Olita, A., Sorgente, R., Natale, S., Gaberšek, S., Ribotti, A., Bonanno, A. and Patti, B. (2007) Effects of the 2003 European heatwave on the Central Mediterranean Sea: surface fluxes and the dynamical response. *Ocean Science*, **3**, 273–289.

Oliver, E.C.J., Donat, M.G., Burrows, M.T., Moore, P.J., Smale, D.A., Alexander, L.V., BenthuySEN, J.A., Feng, M., Sen Gupta, A., Hobday, A.J., Holbrook, N.J., Perkins-Kirkpatrick, S.E., Scannell, H.A., Straub, S.C. and Wernberg, T. (2018) Longer and more frequent marine heatwaves over the past century. *Nature Communications*, **9**, 1324.

Oliver, E.C.J., BenthuySEN, J.A., Darmaraki, S., Donat, M.G., Hobday, A.J., Holbrook, N.J., Schlegel, R.W. and Sen Gupta, A. (2021) Marine heatwaves. *Annual Review of Marine Science*, **13**, 313–342.

Patil, G.P. and Taillie, C. (2003) Geographic and network surveillance via scan statistics for critical area detection. *Statistical Science*, **18**, 457–465.

Pfleiderer, P., Nath, S. and Schleussner, C.F. (2022) Extreme Atlantic hurricane seasons made twice as likely by ocean warming. *Weather and Climate Dynamics*, **3**, 471–482.

Ronneberger, O., Fischer, P. and Brox, T. (2015) U-net: convolutional networks for biomedical image segmentation. In *Medical image computing and computer-assisted intervention–MICCAI 2015: 18th international conference*, Munich, Germany, Oct. 5th–9th, pp. 234–241. Springer International Publishing.

Tango, T., and Takahashi, K. (2005) A flexibly shaped spatial scan statistic for detecting clusters. *International Journal of Health Geographics*, **4**, 11.

Venkatraman, E. (1992) Consistency results in multiple change-point problems, Ph.D. Thesis, Stanford University.

Verzelen, N., Fromont, M., Lerasle, M., and Reynaud-Bouret, P. (2023). Optimal change-point detection and localization. *The Annals of Statistics*, **51**, 1586–1610.

von Schuckmann, K., Moreira, L., Cancet, M., Gues, F., Autret, E., Aydogdu, A., et al. (2024) The state of the ocean in the northeastern Atlantic and adjacent seas. *State of the Planet*, **4**, 1–32.

Vostrikova, L. (1981) Detection 'disorder' in multidimensional random processes. *Soviet Mathematics Doklady*, **24**, 55–59.

Wan, Q., Gao, L., Li, X., and Wen, L. (2022) Unsupervised image anomaly detection and segmentation based on pretrained feature mapping. *IEEE Transactions on Industrial Informatics*, **19**, 2330–2339.

Wang, T. and Samworth, R. J. (2018) High dimensional change point estimation via sparse projection. *Journal of the Royal Statistical Society Series B: Statistical Methodology*, **80**, 57–83.

Wang, H. and Song, M. (2011) Ckmmeans.1d.dp: optimal k-means clustering in one dimension by dynamic programming. *The R Journal*, **3**, 29–33.

Wang, D., Yu, Y. and Rinaldo, A. (2020) Univariate mean change point detection: Penalization, CUSUM and optimality. *Electronic Journal of Statistics*, **14**, 1917–1961.

Yao, Y.-C. (1988) Estimating the number of change-points via Schwarz' criterion. *Statistics and Probability Letters*, **6**, 181–189.

Yu, Y., Madrid, O. and Rinaldo, A. (2022) Optimal partition recovery in general graphs. In *International Conference on Artificial Intelligence and Statistics*, PMLR, pp. 4339–4358.

Zhang, Z., Assunçāo, R., and Kulldorff, M. (2010) Spatial scan statistics adjusted for multiple clusters. *Journal of Probability and Statistics*, **2010**, 642379.

Zhao, Z., Ma, T. F., Ng, W. L. and Yau, C. Y. (2024) A composite likelihood-based approach for change-point detection in spatio-temporal processes. *Journal of the American Statistical Association*, **119**, 3086–3100.

Zheng, C., Eckley, I. A. and Fearnhead, P. (2022) Consistency of a range of penalised cost approaches for detecting multiple changepoints. *Electronic Journal of Statistics*, **16**, 4497–4546.

Supplementary Material for “Optimal Spatial Anomaly Detection”

Baiyu Wang and Chao Zheng

A Non-separable spatial anomalies

In Section 3 we show that spatial anomaly regions can be consistently detected when they are sufficiently separated, as specified in Assumption 2(iii). In practice, however, this assumption may be violated, for example, when anomaly regions share part of their boundaries or when one region is nested within another. In this section, we consider spatial anomaly detection without imposing Assumption 2(iii), while preserving consistent detection guarantees and the same localisation rate. To this end, we need to make a stronger assumption on the regional signal difference. Recall in Section 3, we define Δ as the minimum mean difference between any anomaly region and the baseline. In this section, we change its definition as

$$\Delta := \min_{\substack{i \neq j \\ i, j = 0, \dots, m^*}} |\mu_i^* - \mu_j^*|,$$

where we also consider pairwise mean signal difference between any anomaly regions, i.e., $\Delta_{i,j} := |\mu_i^* - \mu_j^*|$. The updated detectability assumptions are as follows:

Assumption A.1. (i) *There exists $\eta > 0$ such that*

$$\frac{\Delta^2}{\sigma^2} \geq C_\eta \cdot \frac{\log^{1+\eta} n}{\sqrt{n}},$$

where $C_\eta > 0$ is a constant.

(ii) *Same as Assumption 2(ii).*

(iii) *For any $i, j \in \{1, \dots, m^*\}$ and $i \neq j$, there exist constants C_{low} and C_{up} satisfied*

$$C_{low} \cdot \Delta \leq \Delta_{i,j} \leq C_{up} \cdot \Delta.$$

Similar to Section 3, Assumption A.1(i) and (ii) impose a lower bound on the SNR. Assumption A.1(iii) is an additional assumption that constrains the scale of mean signal differences.

Relaxing Assumption 2(iii) removes constraints on the distance between anomaly regions, therefore the regional penalty is no longer necessary. We can obtain an estimator by minimising the classic L_0 penalised cost function, i.e.,

$$\{\hat{m}; \hat{R}_{1:\hat{m}}\} = \arg \min_{m; R_{1:m} \in \mathcal{R}} (L(R_{1:m}) + \beta m), \quad (\text{A.1})$$

which is similar to the timeline setting, where \mathcal{R} is defined as the class of smooth regions in Definition 2.

The following Theorem A.1 shows that solving (A.1) yields consistent estimators of the spatial anomaly regions, with localisation error at rate $O(\sqrt{n} \log n)$.

Theorem A.1. *Suppose Assumptions 1, 3(i) and A.1 hold. If we choose $\beta = C_{\beta,3}\sqrt{n} \log n$, where $C_{\beta,3}$ is a large enough absolute constant not depending on n and m^* . Let $\{\hat{m}; \hat{R}_{1:\hat{m}}\}$ be the minimiser from solving (A.1). There exist constants $c_\gamma, C_{\varepsilon,3} > 0$ such that*

$$\hat{m} = m^* \quad \text{and} \quad D\left(\hat{R}_j, R_j^*\right) \leq \frac{C_{\varepsilon,3}\sigma^2}{\Delta^2} \sqrt{n} \log n, \quad j = 1, \dots, m^*$$

holds with probability at least $1 - 2 \exp(-c_\gamma \sqrt{n} \log n)$.

B Additional simulations

We report additional simulations for 2-dimensional independent data at sample size $n = 1225$ as a supplement to Section 7.1. We examine the same 2D settings as in Section 7, with 9 different SNR combinations and applying the same parameter selection criterion from Section 7.1. The results are summarised in Table S1 and Figure S1.

		$n = 1225$								
		Setting 1			Setting 2			Setting 3		
Δ	$ R $	125	180	245	53	99	153	52	75	101
		1	32	34	53	19	23	36	20	24
NoC(%)	2	62	74	88	21	52	74	55	81	83
	3	97	100	100	76	100	100	100	100	100
	1	31	31	11	—	23	34	—	—	—
Err(%)	2	27	26	32	10	7	15	—	—	—
	3	30	26	17	1	17	12	8	32	32
	1	62	59	57	93	74	69	142	123	112
DPLS-SAD	2	22	21	20	35	34	31	88	76	76
	3	10	10	9	17	17	16	41	38	36
	1	42	44	51	—	56	55	—	—	—
DCART	2	30	32	36	42	40	40	—	—	—
	3	25	30	35	33	28	27	130	124	110

Table S1: Performances of DPLS-SAD and DCART. “—” denotes that DCART estimates all the points as baseline in more than 95% simulations. In Settings 3, with $\Delta = 1$, we scale both β and λ by factors of 0.65.

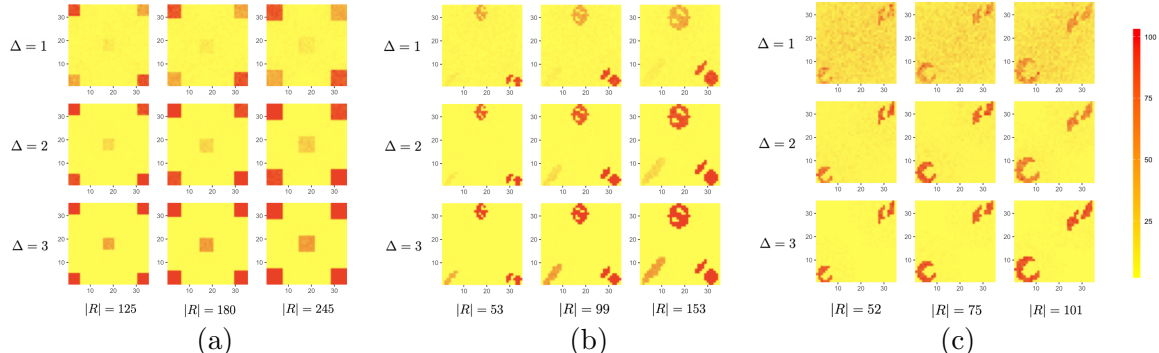


Figure S1: Frequency of points detected as anomalies, varying by 3 settings, with sample size $n = 1225$. Each setting includes 9 combinations of Δ and $|R|$ (top to bottom, Δ increasing; left to right, $|R|$ increasing).